EDGE ARTICLE

Non-close-packed pore arrays through one-step breath figure self-assembly and reversal†

Aaron Zhenghui Thong, Daniel Soon Wei Lim, Aniq Ahsan, Glen Tai Wei Goh, Jianwei Xu and Jia Min Chin*

Non-close-packed arrays of micro- and submicron-pores with separation distances many multiples of pore size were fabricated using a dynamic self-assembly method known as breath figure patterning. We report a novel method by which these arrays can be formed *via* the *in situ* control of growth and shrinkage of the water droplet arrays during polymer film drying. Transfer of the polymer solution onto a thermally conductive stage midway during the drying process afforded breath figure arrays with feature separation-to-size ratios of up to 12.44. This novel approach introduces the possibility of forming non-close-packed morphologies not typically accessible *via* traditional self-assembly methods.

Introduction

The ability to spontaneously organize micro- and nanoscale architectures *via* localized non-covalent interactions is a strong motivation for developing self-assembling systems. Despite the advances in these methods, generating micro-scale architectures with large feature separation-to-size ratios has remained generally inaccessible *via* such bottom-up approaches due to their high energy configurations. Non-close-packed (NCP) structures offer additional benefits over their close-packed (CP) analogues such as forming improved photonic band-gap materials[1] and the reduction of "cross-talk" in assays due to the increased separation between adjacent analytical sites.[2,3] In order to fabricate such NCP arrays, most strategies involve the initial fabrication of CP colloidal crystal arrays followed by a post-synthetic step. These steps include reactive etching,[4,5] solvent or mechanical swelling[6,7] and photolithographic techniques.[8–10] Requiring additional post-synthetic steps to fabricate these architectures erodes a significant advantage of self-assembly processes, in that it avoids multiple fabrication steps thus making the process more cost-effective.

For particles to self-assemble in an NCP manner, some repulsive force (*e.g.* electrostatic interactions)[3,11] must exist between adjacent particles or an energy barrier preventing their aggregation. The breath figure (BF) method, like colloidal-crystal-based methods, relies on attractive forces to aggregate porogen particles (condensed water droplets), of which close-packing leads to hexagonal ordering of the eventual array.[12] However, this does not provide inter-particle repulsive forces required for the formation of NCP arrays. This is well known in literature as most, if not all, of the work utilising the BF method have focused on the creation of CP arrays for the templation of various thin film materials.[13–19] In the BF method, evaporative cooling of the solution surface *via* solvent vaporization drives condensation of atmospheric water. Assembly of porogen droplets is then due to convection, Marangoni and thermocapillary forces, typically resulting in a hexagonal CP structure. Despite the tendency of these forces to destabilize NCP arrangements of water droplets by droplet aggregation into rafts and islands,[20–22] we nonetheless observed NCP arrays at the periphery of typical CP breath figure arrays (BFAs) synthesized *via* a modified spatio-thermal templating method[23] (Fig. 1, refer to Fig. S1† for details of method). Voronoi analysis of the NCP BFA shown in Fig. 1F (low-magnification image can be found in the ESI, Fig. S3† (top)) showed positional and coordinational correlation with a coordinational entropy ($-\sum P_n \ln(P_n)$) of 0.926, similar to that of some CP BFAs reported in the literature[24] (perfectly ordered features give a 0 value while randomly arranged features give a value of 1.657, see Fig. S2 and Table S1†). These NCP arrays formed typically extended for lateral dimensions of a few hundred μm and even up to the mm scale (see Fig. S3†).

In light of these observations, we decided to investigate the formation of these NCP BFAs and hereby propose a mechanism by which these arrays can be stabilized. We then demonstrate a proof-of-concept by exploiting the dynamic nature of the BF method to allow the self-assembly of condensed water droplets into a periodic NCP pattern.

Institute of Materials Science and Engineering (IMRE), 3 Research Link, Singapore 117602. E-mail: chinjm@imre.a-star.edu.sg
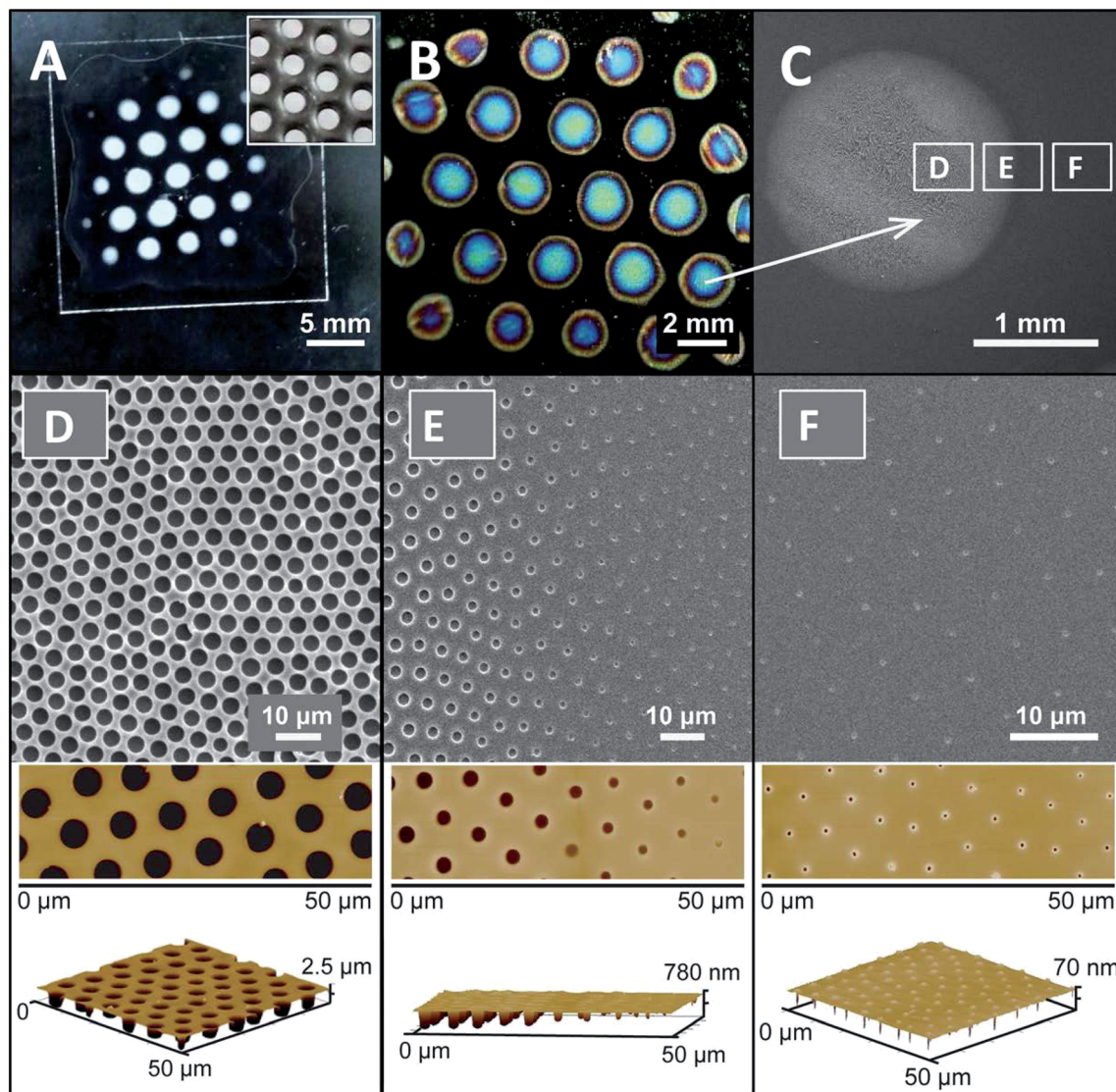
Fig. 1 Photographs of a patterned film (using spatio-thermal templating) seen against (A) a black surface (inset: patterned stage used) and (B) against a light source (brightness tone curve adjusted with Image Data Converter). (C) Low magnification scanning electron micrograph of the arrays, rectangles drawn illustrate representative regions where (D) CP, (E) gradient and (F) NCP BFAs were found. (D–F) SEM (top) and AFM (bottom) images displayed for the corresponding arrays.
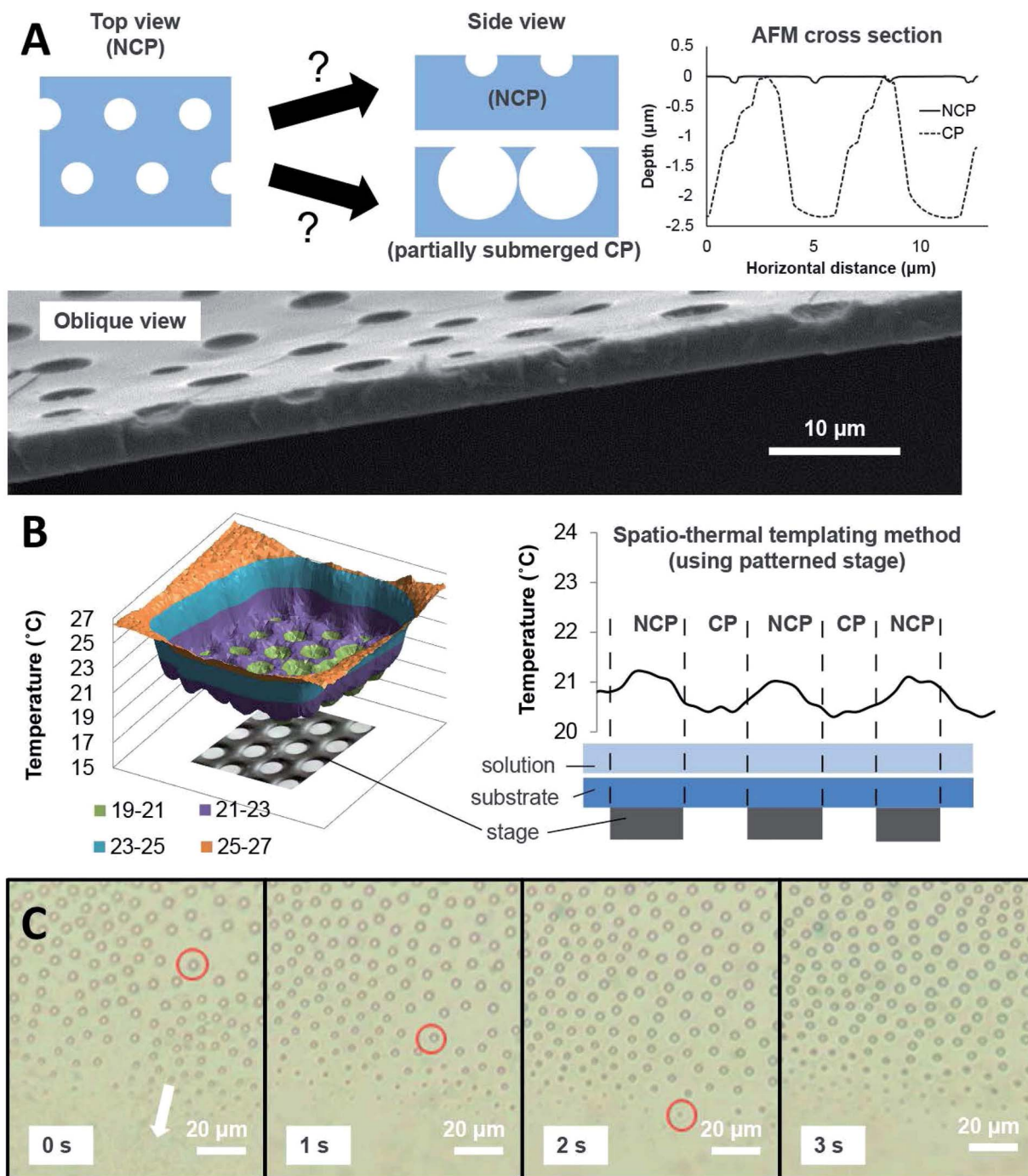
Results and discussion

Investigation into NCP BFA formation

We first eliminated the possibility that the observed NCP architectures were simply surface artifacts of partially submerged CP arrays (Fig. 2A, top left) by performing cross-sectional scanning electron microscopy (SEM) and atomic force microscopy (AFM). AFM evidence showed that the NCP feature depth was ~100 nm as compared to the µm-scale depth of the CP arrays (Fig. 2A, top right). This was corroborated by cross-sectional SEM which showed that the droplet array had crystallized in a periodic NCP fashion, with no sub-surface hard-sphere packing interactions (Fig. 2A, bottom).

Under the conventional BF mechanism, it is easy to assume that these small distributed droplets (Fig. 1F) were a result of random nucleation processes before growth and close-packing by Marangoni forces can take place, resulting in CP architectures as found in Fig. 1D. However, the random nucleation process is generally observed to be disordered and should not give rise to long-range order. Such order would require some form of "communication" between particles (or nucleation sites) at large distances (10–100 µm) not typically observed in nucleation mechanics. Several mechanisms have been previously put forth to explain the separation (i.e. non-coalescence) of water droplets floating on some liquid surface. These include the replenishment of a solvent vapor layer[25] or the presence of a thin polymer lining[26] separating individual droplets. However, none of the current postulated mechanisms provide a satisfactory explanation for both the positional and orientational order at the large scale separation seen in the NCP BFAs.

Fig. 2 Evidence for porogen reversal. (A) Top left: a periodic NCP surface architecture from the top view may be formed by a partially submerged CP array as revealed by the side view. Top right: AFM plot of the representative cross-sectional depth of CP (dotted line) and NCP (solid line) BFAs. Bottom: cross-sectional SEM of a freeze-fractured sample revealed no sub-surface packing interaction between adjacent features in the NCP array. (B) Left: influence of the patterned stage on solution surface temperature during drying (spatio-thermal templating method). Right: an illustrative cross section of the thermal profile. Typical array types (NCP/CP) found in each region are shown above the graph. (C) Real-time optical microscopy showed water droplets shrinking (a single droplet is circled for clarity) as they were pushed along by the convection current (direction of motion indicated by the white arrow). After 3 seconds, the water droplet had shrunk below the resolution of the optical microscope (see Movie S1†).

We have found that these tiny droplets are, unexpectedly, *not* a product of the pre-growth nucleation mechanism, but a rather separate mechanism altogether. Real-time optical microscopy revealed that these tiny droplets are formed due to the shrinking of larger water droplets (Fig. 2C). Two questions then arise here: *why* do these water droplets shrink, and by extension, *how* do they shrink while maintaining the overall hexagonal order of the original CP BFA?

The first question can be answered from thermal measurements of the system during BF formation. Thermal

measurements during BFA formation indicated that these peripheral regions encountered higher local temperatures (reduced evaporative cooling effect) during the casting process due to heat transfer from the metal stage beneath (Fig. 2B). The temperature gradient formed results in several effects. Firstly, mass-flow of the solvent occurs in the direction of these warmer areas, bringing with it close-packed BF rafts floating on its surface (similar to the convective flow responsible for "coffee-rings").[27] The direction of flow observed during real-time optical microscope confirms this fact (Fig. 2C). Secondly, we hypothesized that these CP arrays of water droplets reverse their growth when moved into a warmer local environment. Cai and Zhang have demonstrated that water droplets which form on a solid surface can grow or shrink when placed under humid or dry airflow respectively.[28] In a similar manner, a change in temperature could induce shrinking of the droplets. We show a proof-of-concept of this phenomenon (termed "BF reversal") in the following chapter.

The second question is perhaps more important, since the long-distance ordering of the NCP BFAs is of greater interest to us. The presence of transition morphologies in Fig. 3 grants insight into how the long-range order may be achieved. Such morphologies appear to be formed by a smaller droplet trapped within the "fossilized" remains of its larger precursor droplet. This is due to the inability of the matrix walls to completely re-mold around the shrunken porogen. The energy requirement for polymer matrix re-molding during the reversal process provides a convenient mechanism by which we can then explain the retention of hexagonal order.

Due to the mass-flow movement of BFAs into the reversal regime, we can observe snapshots of the transition process from CP to NCP arrays. Fig. 3A–C illustrate how this occurs. BFAs which are transferred earlier (indicated in red) would have undergone reversal in a polymer matrix with the highest solvent content (lowest viscosity). This allows for complete re-formation of the polymer walls and hence forms the eventual NCP BFA. The final morphology corresponds to the distance from the edge of the BF patterns. Moving from 3D to 3G (*i.e.* farther from the edge), we observed a transition from NCP to homocentric pore-in-pore to eccentric pore-in-pore type morphologies, corresponding with that expected from BF reversal in an increasingly viscous medium.

Proof of concept

Traditionally, efforts to utilize the BF method in polymer film patterning only focused on adjusting initial parameters of the system (humidity, airflow, solvent/polymer species *etc.*)[13–16,29–32] Recently, Noorduin *et al.* showed that dynamic changes in the environment during self-assembly can allow access to bottom-up design of complex crystal morphologies.[33] Unlike colloidal templates, where the template size is fixed, here, the porogen size can be dynamically modified during the self-assembly process since its nucleation and growth occur in response to environmental conditions.[13,20]

As a proof-of-concept, we proceeded to actively induce dynamic reversal of porogen growth *in situ* by modification of the system parameters during self-assembly. Polystyrene/CHCl$_3$ solution was first cast on a glass cover slip (substrate) suspended over an air pocket and the resultant condensed water droplets were left to pack in an orderly CP pattern. At a set time after solution casting (0, 15, 30, 45, and 60 seconds), the solution surface temperature was rapidly raised by transferring the substrate onto a silicon stage, which acted as a heat reservoir for the remainder of the drying process. It was expected that the porogen would evaporate as a dynamic response to the change in solution temperature and that the re-formation of the polymer matrix around the shrinking droplets would finally yield self-assembled NCP architectures (see Fig. 4 for illustration).

The time-resolved thermal profile of the solution surface using this method shows two distinct regimes (Fig. 4A): a pre-transfer step where the liquid surface temperature, $T_{surface}$, decreases and remains lower than the dew point, T_{dew}, and a post-transfer step where $T_{surface}$ increases and remains above T_{dew}. We predicted that the eventual feature separation distances (S, measured center-to-center) would correlate to the initial growth of the droplets prior to transfer since net condensation occurs when $T_{surface} < T_{dew}$. To quantify this growth, we defined a growth factor, α, based on the condensation rate of water vapor (ignoring coalescence effects). In a simplified model of condensation, the rate of growth of water droplets at a point on a liquid surface is proportional to the difference in saturation vapor pressure between the atmosphere ($p(T_{dew})$) and the liquid surface ($p(T_{surface})$), assuming constant concentration gradient in the boundary layer and mass diffusivity.[34] The saturated vapor pressure can be expressed based on the Magnus approximation[35] with recommended coefficients by Alduchov–Eskridge ($A = 17.625$, $B = 243.04\ °C$).[36] This is given by:

$$p(T) \propto \exp\left(\frac{AT}{B+T}\right) \tag{1}$$

Since $p(T_{surface})$ is itself a function of time, t, the rate of change of the droplet volume can be expressed as:
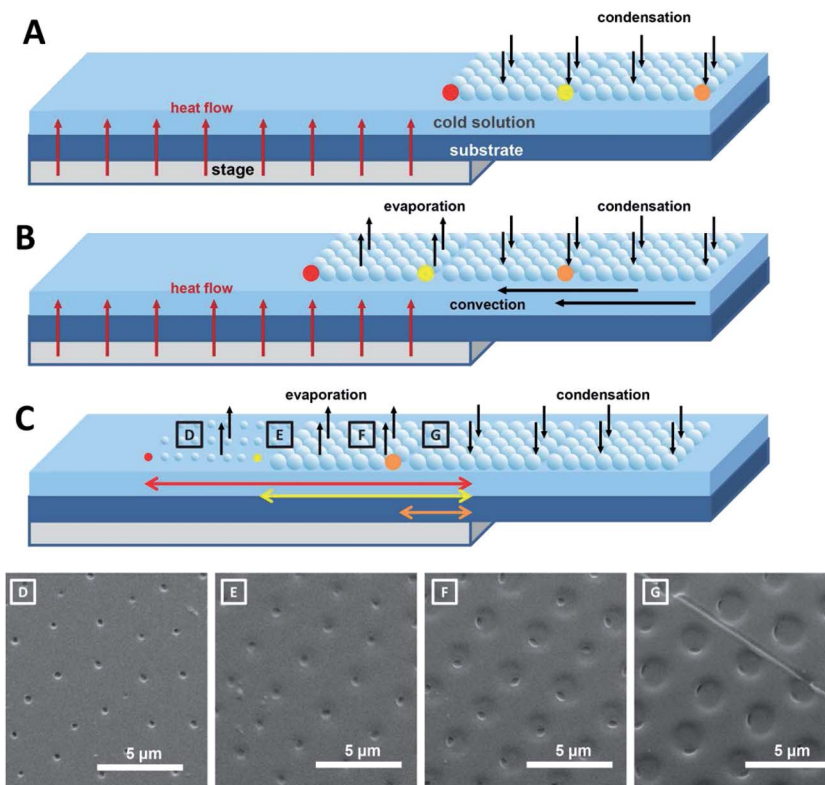
$$\frac{dV}{dt} \propto \exp\left(\frac{AT_{dew}}{B+T_{dew}}\right) - \exp\left(\frac{AT_{surface}}{B+T_{surface}}\right) \tag{2}$$

The latter function is represented as $f(T_{surface}(t))$.

$$f(T_{surface}(t)) \equiv \exp\left(\frac{AT_{dew}}{B+T_{dew}}\right) - \exp\left(\frac{AT_{surface}}{B+T_{surface}}\right) \tag{3}$$
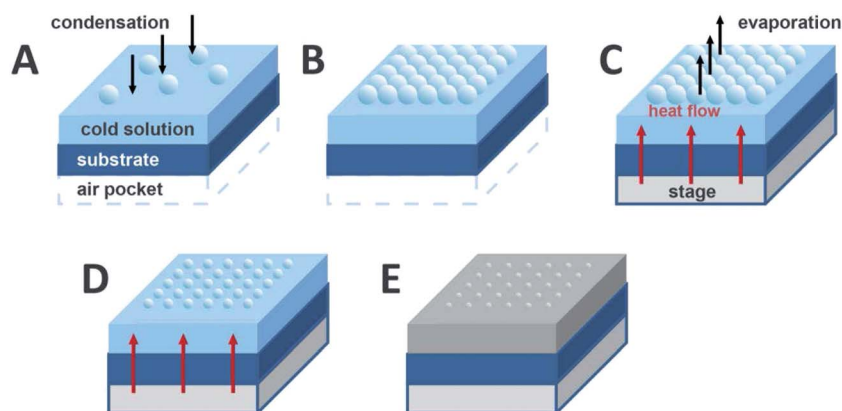
$$\frac{dV}{dt} \propto f(T_{surface}(t)) \tag{4}$$

It then follows that when $T_{surface} < T_{dew}$ in the pre-transfer step, $|T_{surface}(t)|$ is positive; net condensation occurs and the water droplets grow ($dV/dt > 0$). To verify that porogen growth (and hence BF formation) only occurs when $T_{surface} < T_{dew}$, a negative control was performed in which the glass cover slip was set on a thermally conductive stage from the start (*i.e.* transferred at 0 s). The thermal profile showed that the solution surface temperature was consistently greater than T_{dew} throughout the drying process (Fig. S4A†), while optical microscopy and SEM imaging confirmed the absence of any

Fig. 3 Illustration of the formation of transition type morphologies. (A) Condensation occurs at the cooler regions not in contact with the metal stage. (B) These arrays are moved *via* convectional forces to the warmer regions in contact with the stage. (C) Reversal of porogen occurs at different instances. The arrays which are found furthest from the edge (denoted in red) entered at the earliest time and hence started heating back to room temperature the earliest (thereby having the lowest viscosity at the point of re-formation). (D) NCP type arrays are formed when the walls of the initial micro-wells are able to completely re-form around the final droplet where the separation distances are defined by the initial separation of the micro-wells. (E) and (F) Higher matrix viscosity at instance of reversal results in homocentric pore-in-pore morphologies where the final droplets are found closer to the centers of the partially re-formed micro-wells. (G) A highly viscous polymer matrix results in only a slight re-formation of the walls. Eccentric pore-in-pore morphology was observed where the final droplet was found at one side of the micro-wells.

arrays. The absence of BFA growth was also visually observed (*i.e.* solution surface did not turn turbid during drying, indicating the lack of light-scattering features). In view of the linear dependence of the rate of volume growth on $f(T_{surface}(t))$, the

final droplet volume just before transfer is proportional to the integral of $f(T_{surface}(t))$ for the time in which the temperature remains below dew point. We defined t_{start} and t_{end} as the times when the temperature reaches dew point during the cooling and

Fig. 4 Illustration of proposed set-up for formation of NCP BFAs. (A) Initial condensation and growth of water droplets on the cool surface as a result of evaporative cooling during solvent vaporization. (B) Close-packing of the porogen at the solution surface. (C) Introduction of thermally conductive stage causes rapid heating of solution surface. This results in evaporation of porogen as a dynamic response. (D) Water droplet shrinkage occurs while held in place by the polymer matrix. (E) Complete removal of porogen and solvent results in an NCP polymer surface architecture.

heating regimes respectively (see Fig. 5A). The final volume can hence be expressed as:

$$V_{\text{final}} \propto \int_{t_{\text{start}}}^{t_{\text{end}}} f\big(T_{\text{surface}}(t)\big)\mathrm{d}t \qquad (5)$$

As the final separation of the BF features is proportional to the cube root of the final droplet volume just before transfer, it should also be related to the cube root of the integral in eqn (5).

$$S \propto \big(V_{\text{final}}\big)^{1/3} \propto \left[\int_{t_{\text{start}}}^{t_{\text{end}}} f\big(T_{\text{surface}}(t)\big)\mathrm{d}t\right]^{1/3} \qquad (6)$$

The condensation-based growth factor, α, is thus defined as:

$$\alpha \equiv \left[\int_{t_{\text{start}}}^{t_{\text{end}}} f\big(T_{\text{surface}}(t)\big)\mathrm{d}t\right]^{1/3} \qquad (7)$$

As the inhomogeneous drying process affords a range of thermal profiles across the liquid surface, different values of α (and hence S) could be obtained on the same film. Experimentally-determined values of α (across both intra- and inter-film BFA samples) demonstrated good correlation with the corresponding separation distance, S (Fig. 5B), resulting in an
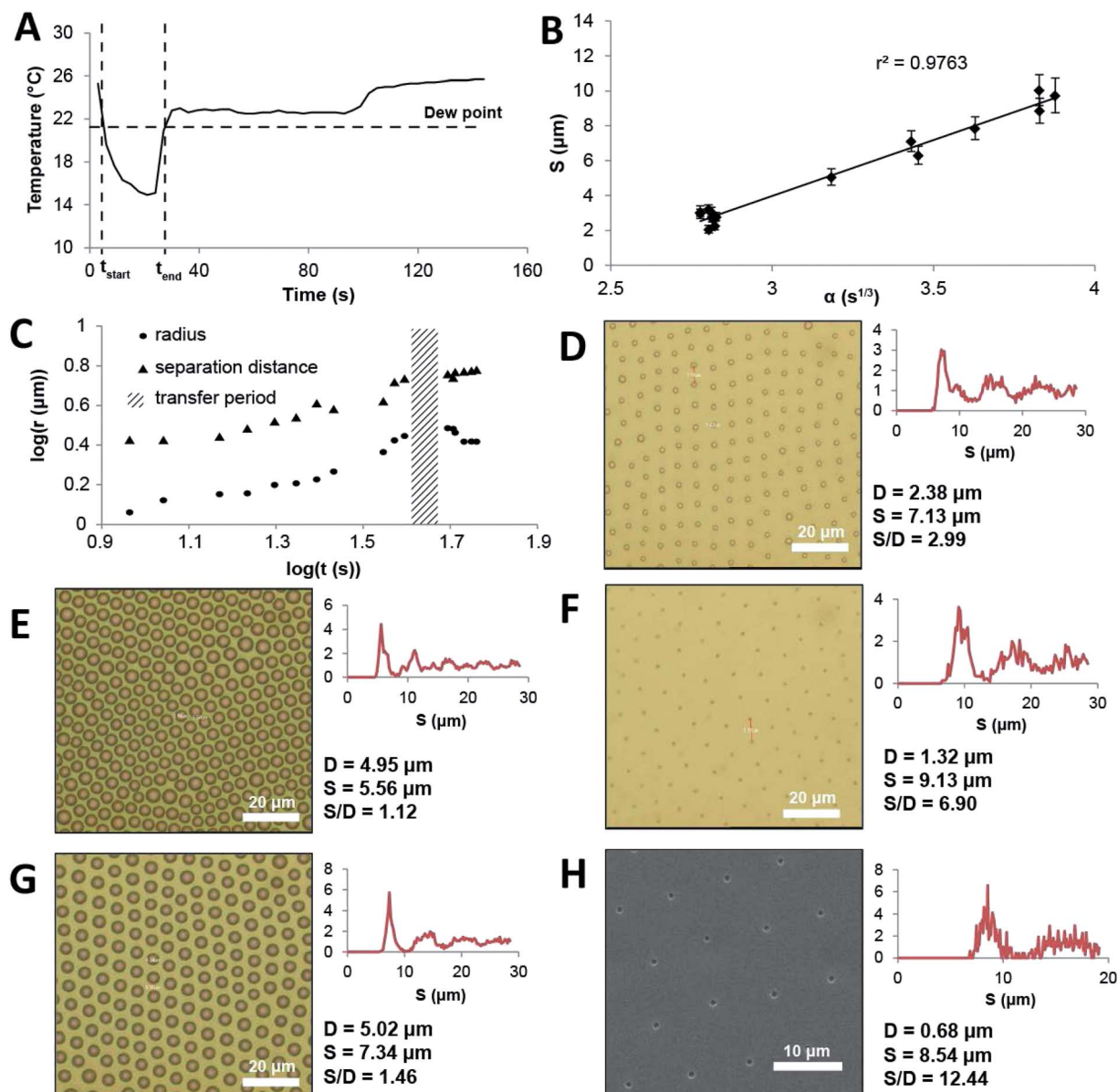

Fig. 5 (A) Typical thermal profile of a representative drying film (sample transferred at 30 s). t_{start} and t_{end} indicate the times where the thermal curve intersects the dew point during temperature decrease and temperature increase respectively. The rest of the thermal profiles can be found in the ESI† (Fig. S4). (B) Linear correlation between separation distance, S and growth factor, α. Error bars represent 1 standard deviation. (C) Time-dependent evolution of the average size/separation distance of BFAs before and after transfer onto the silicon stage measured using real-time optical microscopy. The hatched region indicates when transfer occurs. (D)–(H) Optical micrographs (SEM for (H)) of BFAs with varying S/D ratios by the method illustrated in Fig. 4 (30 s before transfer onto the conductive stage). RDFs, D, S and S/D values are given beside each image. A low-magnification SEM sample can be found in the ESI, Fig. S3† (bottom).

r^2-value of 0.976 (see ESI† for α calculation details). The results show that dynamic intervention in the drying process can be used to tune porogen growth, and eventually BF separation distances. In addition, this allows for the prediction of BF distribution distances through indirect thermal means (*i.e.* through the calculation of the growth factor α). However, tuning of the separation distance is insufficient in itself to form NCP architectures. Porogen reversal also plays an important role. In the second regime (post-transfer), since $T_{\text{surface}} > T_{\text{dew}}$, evaporation dominates and thus water droplet size decreases ($dV/dt < 0$). It is important that the separation distance and order of the porogen particles established in the first regime of growth be maintained through this period of reversal so as to obtain the final periodic NCP arrays. Evidence for this maintenance of separation distance and particle order during the post-transfer reversal step was demonstrated through observation of the condensation process using real-time optical microscopy (Fig. 5C). Both the water droplet radius and separation distance increased during the growth regime. However, upon transfer of the substrate onto a thermally conductive stage, the water droplet radius was observed to decrease (reversing the BF formation), while the droplet separation remained approximately constant, thereby forming NCP BFAs. This observation that the final separation distance is independent of the post-transfer reversal process but dependent instead on the pre-transfer growth process corroborated with our earlier findings of the strong correlation between S and α (Fig. 5B).

We were able to obtain BFAs with S/D ratios ranging from 1.12 to 12.44. Radial distribution functions (RDF) of the arrays in Fig. 5D–H showed that the features maintained a distinct separation distance as evidenced by the presence of a sharp first peak in the RDF. The fact that this nearest-neighbor ordering occurs on a length scale many multiples bigger than the feature size proves that water droplets can be stabilized in an NCP fashion *via* thermally-controlled porogen shrinkage. Long-range order (beyond nearest-neighbor) was also largely preserved as S/D increased, although defect lines can be observed resulting in the distortion of the hexatic phase to form square and "pearls-on-a-string" type NCP patterns. This is attributed to the re-molding process since the generation of NCP arrays relies on the fluidity of the polymer matrix. Furthermore, excessive reversal precludes the formation of the eventual BFAs as expected. When the cover slip was transferred to the silicon stage too early (<15 s), it resulted in complete matrix re-molding; no ordered arrays were observed in the resulting film by SEM and optical microscopy. This was also observed visually as the turbid surface cleared after the transfer, indicating the loss of light-scattering features.

Conclusion

Investigations into the formation of NCP BFAs indicated that these high energy configurations are formed due to changes in the local microenvironment during the growth and self-assembly process of the porogen. We have shown a proof-of-concept that reversal of porogen growth in the BF method allows unprecedented access into the formation of these periodic NCP pore arrays by synthesizing NCP BFAs with S/D ratios

greater than 10. We show that the seemingly simple BF process can be used to sculpt more complex surface architectures beyond the typical hexagonal CP pore arrays formed in the literature. This novel route further lays the foundation for access to more complex hierarchical architectures (such as pore-in-pore type morphologies) through rational design and control of the dynamic BF process.

Experimental

Materials and methods

Polystyrene (PS) pellets (M_w = 280k) were dissolved in $CHCl_3$ (2% w/w). Ethanol was then added to aliquots of this solution (6% by volume based on the volume of $CHCl_3$). In a typical experiment, 50 µL of the above solution was spread on a glass cover slip in a controlled environment chamber with a humidity controller (ETS dual control 5200). The solution was then left to dry under controlled humidity (75.0 ± 0.5%) at room temperature (25 ± 1 °C). The initial set-up (modified spatio-thermal method) was performed in contact with a patterned metal stage (inset of Fig. 1A). For the proof-of-concept, the cover slip was manually transferred at a set time (0 to 60 seconds) onto a polished silicon wafer to actively induce BF reversal.

Analysis and characterization

Thermal images were captured in real-time using an IR thermal camera (Fluke TI-55). The IR emissivity of the polymer solution was taken to be 0.98 (approximated to that of water). Polymer films were analysed by optical microscopy (Nikon OPTIPHOT2-POL with attached CCD camera) as well as scanning electron microscopy (JEOL JSM 6360LA). Image analysis was performed on ImageJ.[37] Diameters were calculated by assuming each domain or pore to be a proper circle. Separation distances were obtained from the *x*-value of the initial peak in the radial distribution function. Atomic Force Microscopy images were obtained using BRUKER Dimension ICON in tapping mode and analyzed using NanoScope Analysis software. Values of α were calculated *via* a numerical integration method. Coordinational entropies were calculated by considering the value of $-\sum P_n \ln P_n$, where P_n refers to the probability of finding a polygon with n sides in the Voronoi diagram. Monte Carlo simulations were then performed to calculate these entropies using Mathematica 9.

Acknowledgements

References

1 F. Meseguer and R. Fenollosa, *J. Mater. Chem.*, 2005, **15**, 4577–4580.

2 Y. Xia, B. Gates, Y. Yin and Y. Lu, *Adv. Mater.*, 2000, **12**, 693–713.

3 L. Isa, E. Amstad, K. Schwenke, E. D. Gado, P. Ilg, M. Kroger and E. Reimhult, *Soft Matter*, 2011, **7**, 7663–7675.

4 S. Gao, N. Koshizaki, Y. Li and L. Li, *J. Mater. Chem.*, 2011, **21**, 2087–2090.

5 C. H. Sun, W. L. Min and P. Jiang, *Chem. Commun.*, 2008, 3163–3165.

6 X. Yan, J. Yao, G. Lu, X. Li, J. Zhang, K. Han and B. Yang, *J. Am. Chem. Soc.*, 2005, **127**, 7688–7689.

7 Z. Ren, X. Li, J. Zhang, W. Li, X. Zhang and B. Yang, *Langmuir*, 2007, **23**, 8272–8276.

8 J. P. Hoogenboom, C. Retif, E. de Bres, M. van de Boer, A. K. van Langen-Suurling, J. Romijn and A. van Blaaderen, *Nano Lett.*, 2004, **4**, 205–208.

9 C. L. Haynes and R. P. V. Duyne, *J. Phys. Chem. B*, 2001, **105**, 5599–5611.

10 J. C. Hulteen and R. P. V. Duyne, *J. Vac. Sci. Technol., A*, 1995, **13**, 1553–1558.

11 A. M. Kalsin, M. Fialkowski, M. Paszewski, S. K. Smoukov, K. J. M. Bishop and B. A. Grzybowski, *Science*, 2006, **312**, 420–424.

12 D. Y. C. Chan, J. D. Henry and L. White, *J. Colloid Interface Sci.*, 1981, **79**, 410–418.

13 M. Srinivasarao, D. Collings, A. Philips and S. Patel, *Science*, 2001, **292**, 79–83.

14 A. Boker, Y. Lin, K. Chiapperini, R. Horowitz, M. Thompson, V. Carreon, T. Xu, C. Abetz, H. Skaff, A. D. Dinsmore, T. Emrick and T. P. Russell, *Nat. Mater.*, 2004, **3**, 302–306.

15 J. Li, J. Peng, W. Huang, Y. Wu, J. Fu, Y. Cong, L. Xue and Y. Han, *Langmuir*, 2005, **21**, 2017–2021.

16 A. V. Limaye, R. D. Narhe, A. M. Dhote and S. B. Ogale, *Phys. Rev. Lett.*, 1996, **76**, 3762–3765.

17 J. S. Park, S. H. Lee, T. H. Han and S. O. Kim, *Adv. Funct. Mater.*, 2007, **17**, 2315–2320.

18 S. H. Lee, H. W. Kim, J. O. Hwang, W. J. Lee, J. Kwon, C. W. Bielawski, R. S. Ruoff and S. O. Kim, *Angew. Chem., Int. Ed.*, 2010, **49**, 10084–10088.

19 S. H. Lee, J. S. Park, B. K. Lim, C. B. Mo, W. J. Lee, J. M. Lee, S. H. Hong and S. O. Kim, *Soft Matter*, 2009, **5**, 2343–2346.

20 U. H. F. Bunz, *Adv. Mater.*, 2006, **18**, 973–989.

21 M. S. Barrow, R. L. Jones, J. O. Park, M. Srinivasarao, P. R. Williams and C. J. Wright, *Spectroscopy*, 2004, **18**, 577–585.

22 J. Peng, Y. Han, Y. Yang and B. Li, *Polymer*, 2004, **45**, 447–452.

23 M. J. Mullan and P. A. Campbell, *30th Annual International Conference of the IEEE Engineering in Medicine and Biology Society*, Vancouver, Canada, 2008, pp. 2514–2517.

24 E. Ferrari, P. Fabbri and F. Pilati, *Langmuir*, 2011, **27**, 1874–1881.

25 V. Sharma, L. Song, R. L. Jones, M. S. Barrow, P. R. Williams and M. Srinivasarao, *Europhys. Lett.*, 2010, **91**, 38001.

26 O. Pitois and B. Francois, *Colloid Polym. Sci.*, 1999, **277**, 574–578.

27 R. D. Deegan, O. Bakajin, T. F. Dupont, G. Huber, S. R. Nagel and T. A. Witten, *Nature*, 1997, **389**, 827–829.

28 Y. Cai and B.-M. Z. Newby, *Langmuir*, 2009, **25**, 7638–7645.

29 J. Aitken, *Nature*, 1911, **86**, 516.

30 G. Widawski, M. Rawiso and B. Francois, *Nature*, 1994, **369**, 387–389.

31 A. Steyer, P. Guenoun, D. Beysens and C. M. Knobler, *Phys. Rev. B: Condens. Matter*, 1990, **42**, 1086–1089.

32 L. Song, V. Sharma, J. O. Park and M. Srinivasarao, *Soft Matter*, 2011, **7**, 1890–1896.

33 W. L. Noorduin, A. Grinthal, L. Mahadevan and J. Aizenberg, *Science*, 2013, **340**, 832–837.

34 D. Beysens, A. Steyer, P. Guenoun, D. Fritter and C. M. Knobler, *Phase Transitions*, 1991, **31**, 219–246.

35 G. Magnus, *Ann. Phys. Chem.*, 1844, **137**, 225–247.

36 O. A. Alduchov and R. E. Eskridge, *J. Appl. Meteorol.*, 1996, **35**, 601–609.

37 C. A. Schneider, W. S. Rasband and K. W. Eliceiri, *Nat. Methods*, 2012, **9**, 671–675.